Springer

Available online at https://link.springer.com/journal/42241
http://www.jhydrodynamics.com
Journal of Hydrodynamics, 2026, 38(4): 678-695
https://doi.org/10.1007/s42241-026-0068-z

An effective volume mesh deformation approach for hull form optimization based on FFD

Zhi-qiang Liu[1], Shan Wang[1], Xi-yang Liu[1], Jia Su[1], De-cheng Wan[2*]

1. *Shanghai Branch, China Ship Scientific Research Center, Shanghai 200011, China*
2. *Computational Marine Hydrodynamic Lab (CMHL), School of Ocean and Civil Engineering, Shanghai Jiao Tong University, Shanghai 200240, China*

(Received June 3, 2026, Revised July 25, 2026, Accepted July 27, 2026, Published online September 11, 2026)
©China Ship Scientific Research Center 2026

Abstract: Hull form optimization requires numerous numerical calculations to assess the hydrodynamic performance of different hull forms, and generating computational fluid dynamics (CFD) meshes is extremely time-consuming. This study proposes an efficient volume-mesh deformation method based on free form deformation (FFD), enabling fast, complex deformation of numerical volume meshes. This method ensures the consistency of the topological structure of numerical volume meshes across different deformed hull forms, while avoiding the inefficiency of generating a mesh for each deformed hull. Based on the Laplace equation and the OpenFOAM open-source dynamic-mesh library, the boundary-mesh displacement is adaptively transferred to the internal mesh of the computational domain. To verify the efficiency and stability of the self-developed mesh deformation method, three mesh deformation applications are conducted. For hull-form optimization, the resistance of the Japan Bulk Carrier (JBC) is optimized in calm water using the method. By establishing a surrogate model and using a genetic algorithm, a 2.43% reduction in calm-water resistance was achieved, and the efficiency of volume mesh generation improved by approximately 96.8%. No mesh inconsistency or mesh quality issues were observed in the numerical calculation. Through the proposed FFD-based volume mesh deformation method in this study, the foundation is laid for the development of an efficient hull-form optimization framework.

Key words: Hull-form optimization, volume-mesh deformation, free form deformation (FFD), Japan Bulk Carrier (JBC) resistance optimization

0. Introduction

Utilizing hull form deformation tools, several deformed hull forms are obtained based on the initial hull form. To obtain the hydrodynamic performance (e.g. resistance and wake flow) of these deformed hull forms, it is essential to generate numerical volume meshes of the deformed hulls for flow-field calculations. The traditional mesh generation method uses software to produce numerical volume meshes for different deformed hull forms. However, in hull form optimization, generating meshes for each deformed hull form individually significantly reduces the efficiency of ship hydrodynamic shape optimization. It also increases the time consumed for numerical volume-mesh generation.

Additionally, numerical volume meshes of different deformed hull forms may have issues such as inconsistent mesh counts and topological structure[1], as shown in Fig. 1. These problems will increase the uncertainty of numerical optimal results. Therefore, applying the volume mesh deformation method to ship hydrodynamic shape optimization will avoid the above problems while improving its efficiency. Currently, the mainstream mesh deformation methods include the spring analogy method, the Delaunay graph mapping method, the radial basis function method, the support vector regression (SVR) interpolation method, and the inverse distance weight (IDW) method.

The spring analogy method, proposed in 1990, has a core idea: treating each mesh line as an elastic spring. By modeling each edge, the mesh maintains a static equilibrium relationship with one other during movement. The positions of the mesh points after

Project supported by the National Natural Science Foundation of China (Grant No. 52131102).
Biography: Zhi-qiang Liu (1995-), Male, Ph. D.,
E-mail: zqliu012345@163.com
Corresponding author: De-cheng Wan,
E-mail: dcwan@sjtu.edu.cn

movement are obtained by solving the static equilibrium equation in the direction of movement. This method has a simple theory but is not robust when deforming complex meshes, which can easily degrade mesh quality. As a result, the obtained mesh fails to meet the requirements for numerical computation and cannot be used for numerical computation[2]. The Delaunay graph mapping method[3] performs better for volume mesh deformation. It can achieve a wider range of mesh deformation and is highly robust. Its core concept is dividing the computational domain using Delaunay triangles (or tetrahedra). This method maps the computational domain mesh to the Delaunay background mesh and, after deformation, solves for the coordinates of the computational domain mesh points using the local coordinate conservation relationship. However, this method has a relatively complex algorithm. When designing the deformation, manually adding auxiliary points based on experience results in certain usability limitations. The radial basis function (RBF) deformation method is widely used and has extensive applications in both geometric and volume mesh deformation[4]. It performs smooth interpolation of mesh point displacements in space by solving for the coefficients of the mesh basis functions on the object's surface. This method can also achieve large-scale mesh deformation and is highly robust. This complexity results in a significant increase in computational load when deforming large-scale meshes[5]. The SVR deformation method is a mesh deformation interpolation algorithm proposed in 2017[6]. Its core idea is consistent with that of the radial basis function method, but it has looser constraints on the interpolation function. Its coefficients can be obtained by solving a convex quadratic programming problem, rather than a linear system of equations as required by the radial basis function method. Therefore, it has high algorithm efficiency. However, when dealing with large-scale mesh deformation, its ability to control mesh quality is limited, and parameter selection also requires manual experience. The basic idea of the inverse distance weighting (IDW) method[7] is to determine the displacement weight based on the distance to the deformed mesh points, and then to calculate the displacement of each mesh node using the displacement weight. In this way, the boundary deformation is transmitted into the space, generating the corresponding adaptive mesh deformation. This method does not require solving linear or nonlinear systems of equations and adopts explicit calculation. Thus, it has high computational efficiency and can handle large-magnitude mesh deformation.

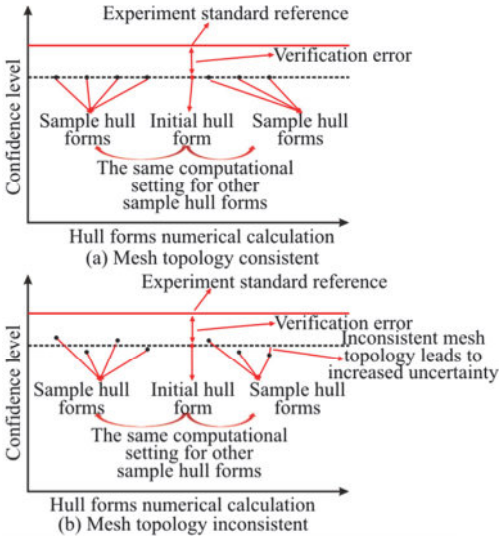


Fig. 1 Increased computational uncertainty due to inconsistent mesh topological relationships

Compared with the field of aerodynamics[8-14], the application of volume mesh deformation and its research on applicability in the optimization of ship hydrodynamic shapes have been relatively limited. On the one hand, the optimization of ship hydrodynamic performance mostly involves multiphase flow, which imposes higher requirements on mesh quality on the other hand, ship structures are relatively complex, demanding high robustness in mesh deformation methods. In recent years, numerous scholars have explored the application of volume mesh deformation in hull form optimization to advance ship hydrodynamic performance optimization technology. Villa et al.[15] used the mesh deformation function in the open-source computational fluid dynamics (CFD) software OpenFOAM to optimize the calm-water resistance of the ship form duisburg test case (DTC). Through mesh deformation, they modified the DTC hull form, achieving a 10% reduction in calm-water resistance. This work indicates that the mesh deformation method has potential applications. Jeong and Jeong[16] compared the effects of mesh deformation in the computational domain using the IDW and RBF methods. The results showed that the RBF-based method had higher mesh deformation efficiency than the IDW method. However, the deformed mesh quality generated by the IDW method was superior to that of the RBF method. Therefore, they further improved the RBF-based volume-mesh deformation method to enhance the quality of the deformed mesh. Based on this improved method, they performed mesh deformation on the bow-line type of the JBC ship form. They optimized its hydrodynamic

performance, verifying the method's feasibility and increasing optimization efficiency by approximately 1/3. Demo et al.[17] employed free form deformation (FFD) and RBF methods to deform the geometric model and volume mesh of the DTC ship. Proper orthogonal decomposition was used to reduce the dimensionality of the design space, thereby improving the efficiency of ship form optimization. A surrogate model was applied to fit mesh deformation non-linearly, enabling self-learning. Finally, through hydrodynamic performance optimization, a 1.2% reduction in the drag coefficient was realized. Nazemian and Ghadimi[18] utilized a gradient-based optimization framework and adopted a discrete adjoint solution approach to optimize the hull lines of a trimaran. The RBF deformation method was used for volume mesh deformation, with the deformation range limited to the hull lines below the waterline. Eventually, a 6.67% reduction in total resistance was achieved. He et al.[19] applied a gradient-based optimization framework to optimize the self-propulsion performance of the JBC ship. The CFD method was used to calculate hull resistance; the virtual propeller disk method was adopted to simulate propeller thrust; and the FFD deformation method was employed to deform the hull surface, combined with the IDW method for volume mesh deformation. The optimization objectives were the stern wake and resistance. Ultimately, 4 optimized ship forms were obtained, achieving a 4.4% reduction in resistance and a 208.0% increase in propulsion efficiency. Li et al.[20] integrated the hull geometric deformation method with the numerical calculation mesh. They directly deformed and reconstructed the hull surface mesh, thereby developing an FFD-based mesh deformation method and an adaptive numerical calculation method. Using this method, the hull lines of a 3 000 TEU research vessel were optimized, with hull resistance as the objective. Finally, the total drag coefficient decreased by 10.8%, indicating a significant reduction in resistance.

The key innovations of this study mark the first application of FFD combined with an OpenFOAM displacement-based Laplace solver to ship multi-objective optimization, while enabling efficient parallel deformation on meshes with millions of cells. This novel approach achieves a significant improvement in hull form hydrodynamic performance optimization efficiency while enhancing the reliability of the obtained optimal results.

1. Mesh deformation approach

1.1 *Mesh deformation theory*

In the field of hull form hydrodynamic optimization, there is a wide variety of deformation algorithms. Commonly used deformation methods include the FFD[21], shifting method[22], and radial basis function method[23]. Most of these methods are applied to the deformation and reconstruction of geometric models, while their applicability to volume mesh deformation remains under further exploration.

Among the above-mentioned methods, the FFD is a geometric deformation method proposed by Parry and Sederberg in 1986[24]. It is used in computer graphics and computational geometry to manipulate and deform three-dimensional geometric objects in a flexible, intuitive manner. The main goal of FFD is to provide a user-friendly method for shape modification that does not require complex mathematical transformations. Initially introduced in computer-aided design, FFD has now been applied across areas such as computer animation, medical imaging, and virtual prototyping.

The core of the FFD method lies in the use of a lattice control volume that encloses the deformable object. By deforming this lattice control volume, the geometric object's shape is indirectly deformed. The advantage of FFD is its ability to provide localized control, enabling users to deform specific regions of interest without affecting the rest of the deformable object. As a relatively traditional deformation method, FFD can be applied to achieve diverse deformations of simple objects.

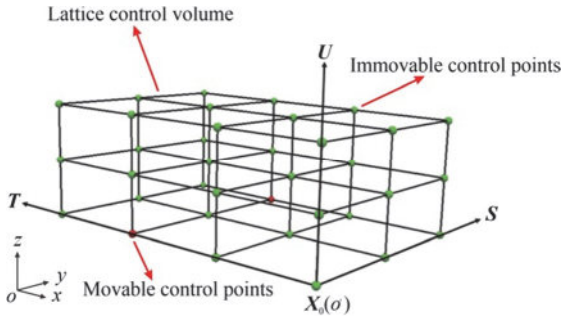


Fig. 2 The local coordinate system of the FFD method

In this paper, further development of FFD has been carried out, enabling it to directly deform the volume mesh of the computational domain in numerical simulations. This avoids the time cost caused by mesh generation for different deformable hull forms. The FFD deformation method mainly achieves deformation by constructing a local coordinate system O'-$\boldsymbol{STU}$, as shown in Fig. 2, where O' is the origin of the local coordinate system, and $\boldsymbol{S}$, $\boldsymbol{T}$, and $\boldsymbol{U}$ are the three vector axes in the local coordinate system, respectively. Suppose there is a point $\boldsymbol{X}$ in the local coordinate system, which can

be described by the coordinates (s,t,u), then point $\boldsymbol{X}$ can be expressed as:

$$\boldsymbol{X} = \boldsymbol{X}_0 + s\boldsymbol{S} + t\boldsymbol{T} + u\boldsymbol{U} \tag{1}$$

where $\boldsymbol{X}_0$ denotes the position of the origin in the local coordinate system. (s,t,u) can be obtained using the following formula:

$$s = \frac{\boldsymbol{T}\times\boldsymbol{U}(\boldsymbol{X}-\boldsymbol{X}_0)}{\boldsymbol{T}\times\boldsymbol{U}\cdot\boldsymbol{S}} \tag{2}$$

$$t = \frac{\boldsymbol{S}\times\boldsymbol{U}\cdot(\boldsymbol{X}-\boldsymbol{X}_0)}{\boldsymbol{S}\times\boldsymbol{U}\cdot\boldsymbol{T}} \tag{3}$$

$$u = \frac{\boldsymbol{S}\times\boldsymbol{T}\cdot(\boldsymbol{X}-\boldsymbol{X}_0)}{\boldsymbol{S}\times\boldsymbol{T}\cdot\boldsymbol{U}} \tag{4}$$

where the value ranges of variables s, t, and u are all $[0,1]$.

Under the local coordinate system O'-$\boldsymbol{STU}$, the lattice control volume is equally divided along the $\boldsymbol{S}$, $\boldsymbol{T}$, and $\boldsymbol{U}$ directions, respectively. Each direction is divided into l, m, and n equal parts, transforming the entire lattice into a mesh composed of several small cubes; the mesh points are the control points on the lattice control volume. The control point $\boldsymbol{Q}_{i,j,k}$. can be expressed as:

$$\boldsymbol{Q}_{i,j,k} = \boldsymbol{X}_0 + \frac{i}{l}\boldsymbol{S} + \frac{j}{m}\boldsymbol{T} + \frac{k}{n}\boldsymbol{U} \tag{5}$$

where $i = 0,1,2,\cdots,l$, $j = 0,1,2,\cdots,m$, $k = 0,1,2,\cdots,n$. Therefore, any point located inside the lattice control volume can be expressed in the local coordinate system using the following formula:

$$\begin{aligned}\boldsymbol{X}(s,t,u) &= \sum_{i=0}\sum_{j=0}\sum_{k=0}\boldsymbol{B}_{i,j}(s)\\ &\cdot\boldsymbol{B}_{j,m}(t)\boldsymbol{B}_{k,n}(u)\boldsymbol{Q}_{i,j,k}\end{aligned} \tag{6}$$

where $\boldsymbol{B}$ denotes the Bernstein polynomial, and its specific formula is expressed as follows:

$$\boldsymbol{B}_{i,n}(u) = \frac{n!}{i!(n-i)!}u^i(1-u)^{n-i} \tag{7}$$

When the control points on the lattice control volume undergo displacement and move to $\boldsymbol{Q}_{i,j,k}$, the coordinate of the new point $\boldsymbol{X}$, denoted as $\boldsymbol{X}_{\mathrm{ffd}}$, is given by:

$$\begin{aligned}\boldsymbol{X}_{\mathrm{ffd}}(s,t,u) &= \sum_{i=0}\sum_{j=0}\sum_{k=0}\boldsymbol{B}_{i,j}(s)\\ &\cdot\boldsymbol{B}_{j,m}(t)\boldsymbol{B}_{k,n}(u)\boldsymbol{Q}'_{i,j,k}\end{aligned} \tag{8}$$

From the above formulas, it can be seen that the FFD deformation method has a simple theory, is easy to use, and can produce various geometric deformations. By setting an appropriate lattice control region to deform the local or the entire geometric object, the smooth transition of the geometric surface is ensured. Therefore, it is also widely used in CAD and computer animation. The following provides an introduction to the theory of volume mesh deformation in the computational domain of numerical simulation.

This method is further developed based on the dynamic mesh method in the open-source CFD software OpenFOAM. The hull surface mesh is deformed using the FFD method, and the Laplace equation (Eqs. (9)-(12)) is adopted to compute the static displacements, whereby the new deformed mesh is obtained. Subsequently, the flow field is solved by the solver on the fixed mesh.

When a mesh point undergoes displacement, the surrounding mesh points must undergo corresponding displacement changes. Such displacement changes are controlled and described using the Laplace equation. For mesh deformation, the general Laplace equation is expressed in three directions as follows:

$$\nabla\cdot(\boldsymbol{\Gamma}_{\mathrm{c}}\nabla\boldsymbol{V}_{\mathrm{c}}) = 0 \tag{9}$$

where $\boldsymbol{\Gamma}_{\mathrm{c}}$ (the subscript c denotes cell-centered) represents the mesh deformation diffusion coefficient, which specifies the rate at which the boundary mesh motion propagates to the internal mesh. $\boldsymbol{V}_{\mathrm{c}}$ denotes the deformation vector field. The selection of $\boldsymbol{V}_{\mathrm{c}}$ can refer to either the mesh displacement or the mesh moving velocity. The selection of $\boldsymbol{\Gamma}_{\mathrm{c}}$ can generally be expressed in a scalar form (The diffusion coefficients in the three directions are the same) or a vector form. During mesh deformation, the solution methods are divided into velocity-based solutions and displacement-based solutions according to the selection of $\boldsymbol{V}_{\mathrm{c}}$.

In the displacement-based solution method, the displacement field at each element's cell center is first calculated. This displacement field is interpolated to all mesh nodes in the computational domain and then added to their initial coordinates to update their positions.

For the velocity-based solution method, the velocity field at the cell center within the mesh element is first computed. This velocity field is then interpolated to the mesh nodes in the computational domain, and the nodes' displacements are obtained by multiplying the velocity by the simulation time step. Essentially, these two solution methods achieve the same goal through different approaches. When solving in the velocity-based manner, Eq. (9) becomes:

$$\nabla \cdot (\boldsymbol{\Gamma}_{\mathrm{c}} \nabla \boldsymbol{U}_{\mathrm{c}}) = 0 \tag{10}$$

where $\boldsymbol{U}_{\mathrm{c}}$ denotes the velocity vector at the cell center of the mesh element in the computational domain. The velocity $\boldsymbol{U}_{\mathrm{p}}$ (subscript p denotes point, referring to mesh nodes) at the mesh nodes is obtained through interpolation. Here, three commonly used interpolation schemes for interpo- lating from the mesh cell centers to the mesh nodes in the computational domain are introduced: linear, upwind, and cubic.

For the displacement-based solution method, Eq. (9) becomes:

$$\nabla \cdot [\boldsymbol{\Gamma}_{\mathrm{c}} \nabla (\Delta \boldsymbol{X}_{\mathrm{c}})] = 0 \tag{11}$$

And the displacement distance $\Delta \boldsymbol{X}_{\mathrm{p}}$ at the mesh nodes is obtained through interpolation. Then the new coordinates of the mesh nodes are:

$$\boldsymbol{X}_{t_{n'}} = \boldsymbol{X}_{t_{n'-1}} + \Delta \boldsymbol{X}_{\mathrm{p}} \tag{12}$$

where $\boldsymbol{X}_{t_{n'}}$ denotes the coordinates of the mesh nodes at time step $t_{n'}$.

After obtaining the motion and deformation of the mesh points on the object boundary within the computational domain, the other mesh points also change accordingly. The positions of the mesh nodes in the computational domain are determined by solving the Laplace equation. The quality of mesh deformation depends on the mesh deformation diffusivity $\boldsymbol{\Gamma}_{\mathrm{c}}$, and this diffusivity $\boldsymbol{\Gamma}_{\mathrm{c}}$ can vary spatially[25]. The commonly used interpolation methods for $\boldsymbol{\Gamma}_{\mathrm{c}}$ are mainly divided into three types: the nearest-neighbor method, the inverse-distance weighting method, and the trilinear interpolation method. The mesh deformation diffusion coefficients $\boldsymbol{\Gamma}_{\mathrm{c}}$ at different positions are obtained through the three interpolation methods mentioned above. Then, by solving the Laplace equation, the displacement deformation corresponding to the volume mesh in the computational domain is derived.

Based on the aforementioned FFD theory, dynamic mesh theory, and mesh quality optimization, a volume mesh deformation method using the FFD approach is developed. The method uses FFD to deform the computational domain, achieving efficient volume mesh deformation while maintaining numerical mesh quality. For hull form optimization, the volume mesh deformation method is used to manipulate the numerical simulation mesh of geometric bodies, thereby indirectly altering the shape of hull surfaces. This enables numerical calculations across different hull forms and avoids the inefficiencies and topological inconsistencies that arise from separately generating meshes for deformed hull surfaces.

1.2 *Mesh-deformation-method applications*

In this subsection, the test and deformation effects of the developed FFD volume mesh deformation method are demonstrated by deforming a numerical simulation mesh for several typical ship and ocean structures. For the deformation test, the 2-D airfoil flow-around mesh and the 3-D David Taylor Model Basin (DTMB) and SUBOFF (the DARPA Suboff submarine model, where DARPA stands for Defense Advanced Research Projects Agency) computational domain mesh are mainly selected.

1.2.1 Deformation of a 2-D mesh

The National Advisory Committee for Aeronautics (NACA) 0012 airfoil was selected for a complex serpentine deformation to compare with the RBF- based volume mesh deformation method[12]. The computational domain mesh and lattice control volume settings are shown in Fig. 3. Ten boundary layers were added using a mesh generation tool, with the first boundary layer set to a height of 3.55×10^{-4} m.

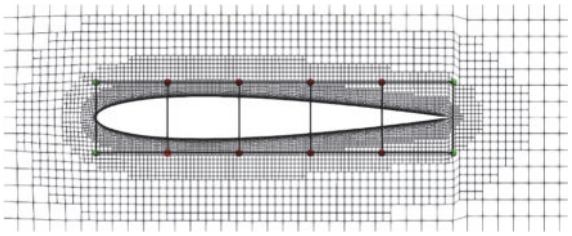


Fig. 3 NACA 0012 wing computational domain mesh and lattice settings

In Fig. 3, the red control points are movable, and an S-shaped mesh deformation is generated by alternately moving them upward and downward. The final mesh deformation is shown in Fig. 4. As the movable control points move, the mesh undergoes a corresponding deformation. The display of the mesh at the leading and trailing edges shows that the boundary-layer mesh on the NACA 0012 airfoil surface exhibits smooth deformation without any mesh distortion.

Compared with the RBF-based volume mesh deformation method developed by Morelli et al.[12], the volume mesh deformation method based on FFD can also achieve complex, stable mesh deformation. Furthermore, the curvature changes in the mesh deformation at the stern are more complex than those in the airfoil deformation studied by Morelli et al., yet the mesh still maintains high quality.

The mesh quality inspection tool was used to check the mesh quality. The results show that the

average non-orthogonal angle of the mesh is 14.551 6 and its maximum skewness is 1.794 8. Both mesh indicators meet the requirements for numerical calculations (For the OpenFOAM numerical simulation platform, its mesh quality requirements specify that the maximum skewness should be below 4 and the maximum non-orthogonal angle should be $70°$).

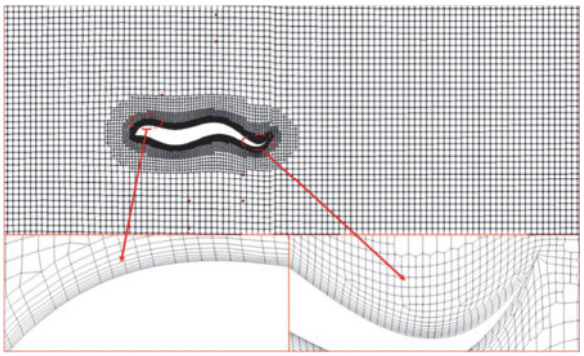


Fig. 4 NACA0012 wing computational domain mesh S-deformation

1.2.2 Volume mesh deformation of the 3-D computational domain for the DTMB hull form

For a complex 3-D computational domain mesh, the DTMB model was selected as the application object. The FFD volume mesh deformation method was used to modify the volume mesh shape of the sonar dome at the bow of the DTMB to test the volume mesh deformation capability for local structures. The model and lattice control volume setup are shown in Fig. 5.

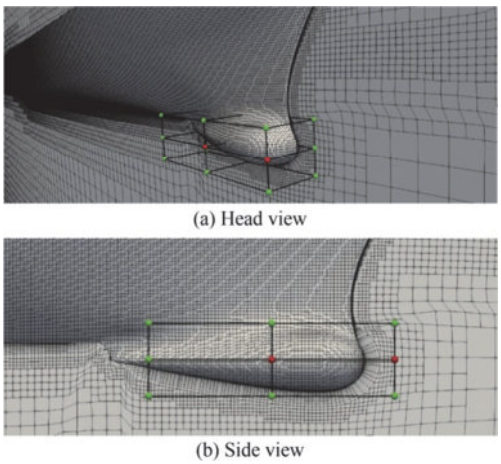


Fig. 5 Schematic of DTMB computational domain mesh and lattice settings

The total number of meshes in the computational domain is 6.83×10^{6}, with 10 boundary layers, and the height of the first boundary layer is 1×10^{-3} m. The volume mesh deformation is achieved by moving the red movable control points shown in Fig. 6, which illustrates the mesh deformation effect on the DTMB hull form computational domain. The figure shows that the boundary layer mesh after deformation still maintains its original characteristic form, without distortion or other anomalies. After the mesh quality inspection, the average non-orthogonal angle is $7.56°$, and the maximum skewness is 1.93. It indicates that, under the maximum deformation condition, the mesh quality remains good both before and after deformation, meeting the requirements for numerical simulation.

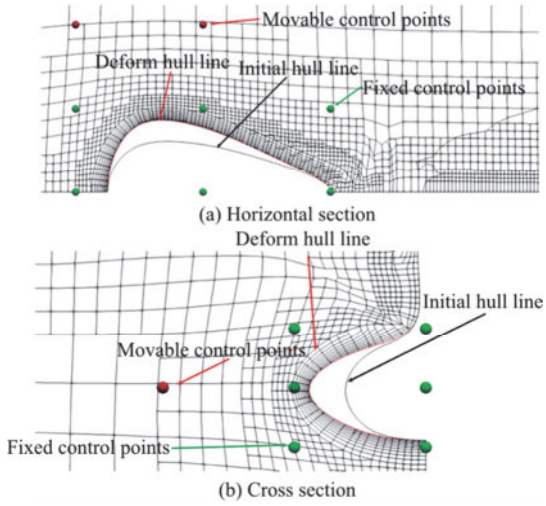


Fig. 6 Schematic diagram of horizontal and cross-sectional mesh deformation of the sonar dome mesh under maximum deformation

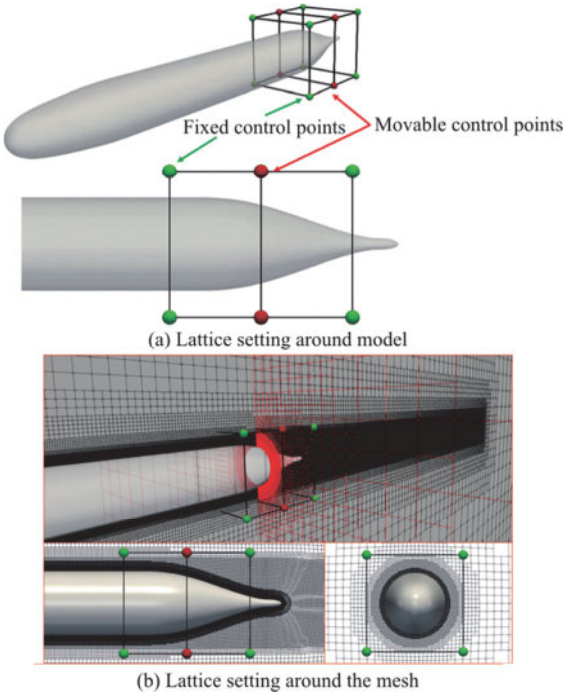


Fig. 7 Stern deformation lattice setting of SUBOFF model and mesh

Table 1 The parallel time cost of the mesh deformation method

Item	Mesh number ($\times10^6$)	Control point number	Deformed mesh number	Time consuming/s
2-D wing	0.012 6	12	30	3.4
DTMB	6.830 0	18	16	310.8
SUBOFF	22.320 0	12	16	776.1

1.2.3 Volume mesh deformation of the 3-D computational domain for SUBOFF

Finally, the SUBOFF was selected as the test sample for mesh deformation. When conducting high-fidelity simulations of underwater vehicles, stringent requirements for wall-adjacent mesh distribution significantly increase the number of meshes. To test the volume-mesh deformation program at the 1×10^9 level, the standard SUBOFF model was selected, with a mesh count of 22.32×10^6 and a height of 8.88×10^{-4} m for the first layer near the wall. The computational domain mesh and lattice control volume setup are shown in Fig. 7, and four control points were used to modify the shape of the SUBOFF's stern form.

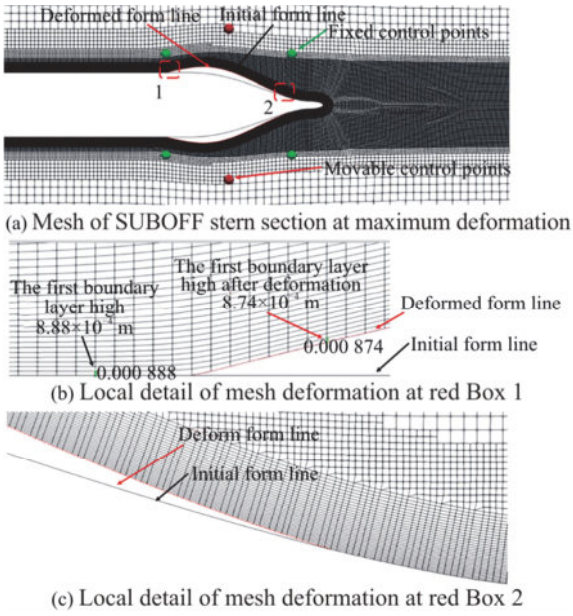


Fig. 8 Mesh deformation of SUBOFF stern form

The mesh at the maximum deformation state was selected for comparative analysis, as shown in Fig. 8. To verify the effect of FFD volume-mesh deformation under conditions of a 1×10^9 level mesh quantity and a fine boundary layer, the deformation smoothness was not controlled. The focus was on the deformation effect of the boundary-layer mesh when deformation folding angles occur. As shown in Fig. 8(b), the height of the first-layer mesh does not change significantly before and after deformation, thereby maintaining the stability of the y^+ (dimensionless wall distance) value during this period. At the same time, the transition of the boundary layer at the folding angles due to deformation proceeds smoothly, ensuring the quality of the boundary-layer mesh. At the maximum deformation, the average non-orthogonality of the mesh is 6.189, and the maximum skewness is 1.162. The maximum values of the above two mesh indicators are consistent with those of the parent computational domain mesh. It maintains the high quality of the parent mesh, and the deformed mesh still meets the requirements of numerical simulation, demonstrating the advantage of the FFD volume mesh deformation method in preserving details.

In addition to ensuring deformation quality, the developed program code also optimizes deformation efficiency. The aforementioned computational domain volume mesh was deformed using an 8-core CPU (model: Intel i7-9700KF, 3.60GHz), and the time consumption under various working conditions is presented in Table 1.

When handling the deformation of a 1×10^9 level mesh, 16 numerical simulation meshes with different forms can be rapidly generated within 13 min. Compared with the traditional approach that requires a single mesh generation per hull form model, this method can improve mesh generation efficiency by several times. Meanwhile, the deformed mesh still meets the requirements of numerical calculations without any deterioration in mesh quality. Before and after deformation, the topological structure of the mesh within the deformed region remains unchanged, therefore, during numerical calculations, calculation stability and reliability will not be significantly affected by changes in topological structures, ensuring mesh consistency in the hydrodynamic numerical simulation of deformed bodies of different marine and offshore structures.

The above application cases demonstrate the potential of the developed FFD volume mesh deformation method in terms of deformation accuracy and efficiency. When conducting numerical optimization for various marine and offshore structures, this method enables rapid construction of a numerical simulation mesh for deformed bodies, while maintaining calculation stability and consistent results.

2. Hull form optimization application

This section primarily focuses on optimizing the

stern lines of the Japan Bulk Carrier (JBC) hull at model scale to improve the stern flow field, thereby reducing resistance and improving propeller inflow quality. Under the constraints of controlling the hull's wetted surface area and displacement, the volume mesh deformation method is used to directly deform the numerical calculation mesh of the initial hull form. On the one hand, this saves the time required to generate meshes of sample hull forms; on the other hand, it maintains consistency in the quantity and topological relationships of the meshes across all sample hull forms, avoiding discrepancies in calculation results caused by mesh-related differences. First, we conduct numerical simulation validation on the initial hull form to obtain a set of high-quality meshes that meet the computational accuracy requirements. Subsequently, the FFD volume mesh deformation program is used to deform the initial hull form mesh, generating sample meshes. A multi-objective surrogate model is constructed based on the multi-objective Kriging theory and combined with the Non-dominated Sorting Genetic Algorithm II (NSGA-II), yielding multiple optimization solutions. Finally, the optimization results are discussed and analyzed, and a conclusion is presented.

2.1 *Benchmark verification*

The JBC hull form at the model scale is selected as the optimization object to test the volume mesh deformation effect and the optimization effect (see Fig. 9). Using the experimental data, the numerical simulation results can be compared with the physical experimental results to verify their accuracy. To be closer to the actual sailing state, the influence of weak wave making on the free surface is considered in the numerical simulation, and the two-phase CFD solver is adopted to perform numerical simulation on the hull flow field. The main model-scale parameters of the JBC hull form are shown in Table 2. The hull speed is 1.179 m/s (the Froude number $Fr = 0.142$).

Table 2 JBC model main parameters

Hull Information	Model scale
Scale ratio, λ	1/40
Length between perpendiculars, L_{pp} / m	7
Maximum waterline beam, L_{WL} / m	1.125
Draft, T_d / m	0.412 5
Molded depth, D / m	0.625
Displacement volume, ∇ / m^3	2.787
Wetted surface area, S_a / m^2	12.223
Block coefficient, C_B	0.858
Longitudinal center of buoyancy (positive forward of midship), $L_{CB}(\%L_{pp})$	2.547 5

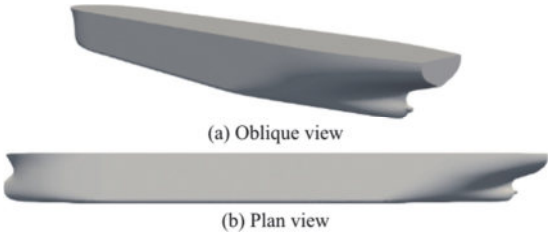


Fig. 9 Schematic diagram of the JBC model

To accelerate the calculation speed and improve computational efficiency, half-domain modeling is adopted for mesh generation. The size of the computational domain is defined as: $-1.5L_{pp} \le x \le 3.0L_{pp}$, $0 \le y \le 1.5L_{pp}$, and $-1.5L_{pp} \le z \le 0.5L_{pp}$, The specific range of the computational domain is illustrated in Fig. 10. The meshing process is implemented using SnappyHexMesh – the built-in meshing tool of OpenFOAM – with the following key mesh controls: the target value of y^+ is set to 40, the height of the first boundary layer mesh is 2.0×10^{-3} m, the number of boundary layers is 6, the expansion ratio of the boundary layer mesh is 1.25. The total mesh count of the computational domain is 6.842×10^6.

The time step size (Δt) is set to 1×10^{-4} s. To accurately capture wave generation and wake flow, local mesh refinement is applied in the stern wake and free-surface regions. The mesh generation at the free surface is shown in Fig. 11.

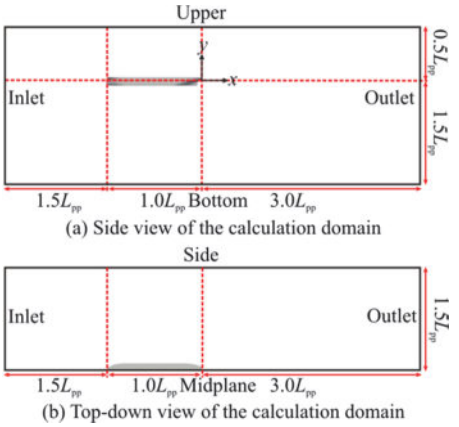


Fig. 10 Computational domain setting

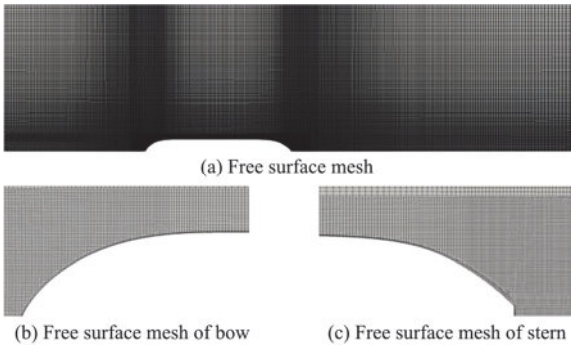


Fig. 11 Mesh around the free surface

Table 3 Comparison of calculation and experiment results of calm-water drag

R_p / N	R_f / N	R_t / N	CFD -C_t	EFD -C_t	Error/%
11.86	26.42	38.28	4.50×10^{-3}	4.29×10^{-3}	4.67

Note: R_p denotes the pressure resistance, R_f denotes the frictional resistance, R_t denotes the total resistance, and C_t represents the total resistance coefficient.

After computation, the final error between the calculated resistance and the experimental value is controlled within 5%, which is comparable to the calculation errors reported in other studies[26-27] (as shown in Table 3). It meets the requirements for ship hydrodynamic shape optimization. In addition to the resistance calculation meeting the accuracy requirement, it can be seen from Fig. 12 that the velocity distribution at each cross-section is in good agreement with the experimental values. Meanwhile, the wake flow is accurately captured, which supports the accuracy of the wake calculation.

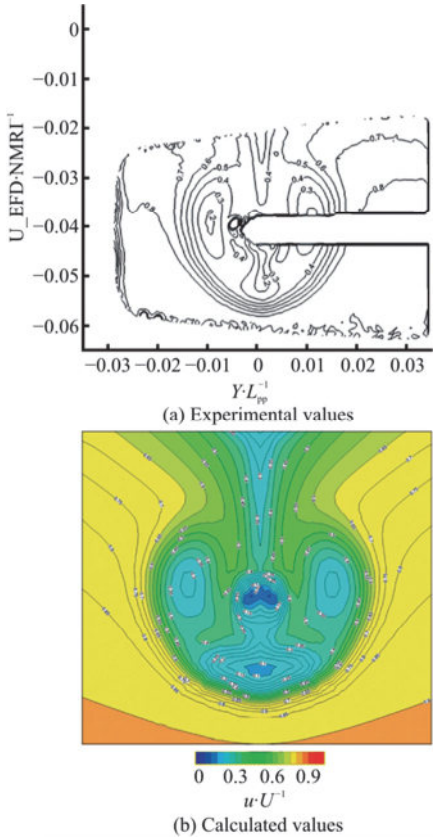


Fig. 12 Comparison of axial velocity distribution at x/L_{pp}=0.984 3

Based on this mesh, mesh convergence verification is conducted. Three sets of meshes (coarse, medium, and fine) are designed, with a mesh size scaling factor of $\sqrt{2}$. The meshes with different resolutions are illustrated in Fig. 13. The total mesh counts are 2.935×10^6, 3.824×10^6, and 18.625×10^6, respectively. Calculations are performed using the same CFD viscous-flow simulation settings, and the final resistance results are presented in Table 4. Through calculation, the mesh convergence factor (R_G) is obtained as 0.42, which falls within the range of 0 to 1. According to the mesh convergence criterion, the mesh is converging. To ensure accurate calculations while maintaining computational efficiency, a medium-scale mesh is used for subsequent numerical calculations.

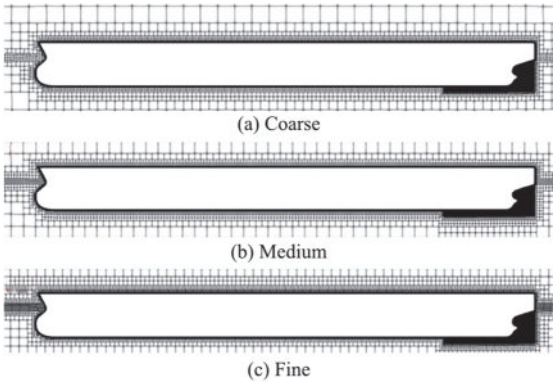


Fig. 13 Three different sizes of computational domain mesh

Table 4 Verification of mesh convergence

Mesh	Mesh number ($\times10^6$)	R_t / N	C_t
Coarse	2.935	40.40	4.76×10^{-3}
Medium	6.824	38.28	4.50×10^{-3}
Fine	18.615	37.32	4.39×10^{-3}
R_G	0.42	0.42	0.42

2.2 *Design of the optimization problem*

In this section, the FFD volume mesh deformation method is used to deform the JBC computational domain mesh, directly yielding numerical meshes of the deformed hulls. Optimization is conducted by taking the JBC hull resistance and the stern wake non-uniformity as optimization objectives, aiming to minimize resistance and propeller inflow non-uniformity W.

$$\min f_{obj}^1 = C_t, \min f_{obj}^2 = W \tag{13}$$

The inflow non-uniformity W of the propeller disk plane is defined as:

$$W = \sqrt{\frac{\sum_{i'=1}^{N}(U_{xi'} - \bar{U}_x)^2}{N}} \tag{14}$$

where i' denotes the i'-th mesh cell on the

propeller disk plane. $U_{xi'}$ represents the axial velocity of the i'-th mesh cell, while $\bar{U}_x$ denotes the average axial velocity at the propeller disk. N stands for the number of mesh cells on the sampled propeller disk. The sampled propeller disk is located at $x/L_{pp}=0.984\,3$, with its center at coordinates (6.890 1, 0, -0.28) and a radius of 0.1 m, as illustrated in Fig. 14. By optimizing these objectives, the JBC hull form with low resistance and high-quality wake is obtained. Meanwhile, the applicability of volume mesh deformation for ship hydrodynamic hull form optimization is verified.



Fig. 14 Wake sampling position (x/L_{pp}=0.984 3)

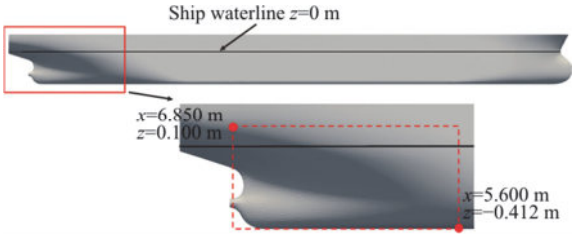


Fig. 15 JBC deformation setting

The deformation region is set at the stern of the JBC. The deformation range is defined as: $5.6\ \text{m} \le x \le 6.85\ \text{m}$, $-0.5625\ \text{m} \le y \le 0.5625\ \text{m}$, and $-0.412\ \text{m} \le z \le 0.1\ \text{m}$, see Fig. 15.

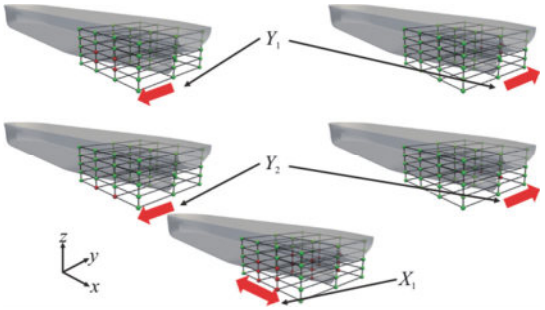


Fig. 16 The movement direction of lattice control points (red control points are movable)

For the selection of design variables, three design variables (deformation parameters) are defined, namely X_1, Y_1, and Y_2. Among them, variables Y_1 and Y_2 control the movement of the volume mesh in the y-direction, while X_1 controls the mesh deformation in the x-direction. The schematic diagram of the deformation region and design variables is shown in Fig. 16.

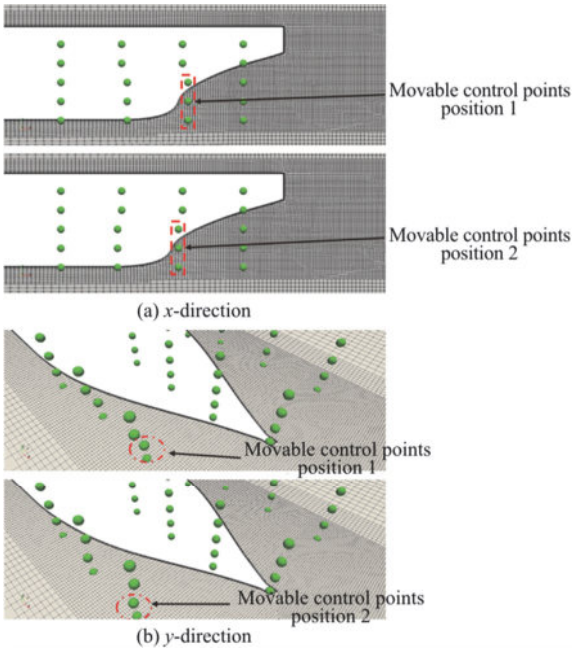


Fig. 17 Mesh deformation in the x- direction and y- direction

The designed lattice control volumes are imposed on the volume mesh of the computational domain. By moving the positions of the lattice control points, the stern lines of the hull are deformed in the x- and y- directions, meanwhile, the surrounding volume mesh of the computational domain automatically updates its mesh coordinates based on the new hull boundary positions, as illustrated in Fig. 17.

The value ranges of the design variables are determined with the hull wetted surface area and displacement constraints taken into account, as shown in Eq. (15). This study is implemented for academic research to validate the practicability of the proposed volume-mesh deformation method in hull-form optimization rather than practical commercial practices. For this reason, the volumetric change arising from hull deformation was not restricted within the threshold of 1%. Finally, the deformation ranges of each design variable are presented in Table 5.

$$\begin{aligned} &\min\ f_{\text{obj}}^{1} = R_{\text{t}}, \\ &\min\ f_{\text{obj}}^{2} = W \ \text{subject to} \left|\frac{S_W - S_{W0}}{S_{W0}}\right| \le 2\%, \\ &\left|\frac{\Delta - \Delta_0}{\Delta_0}\right| \le 2\% \end{aligned} \tag{15}$$

Table 5 The arrangement of design variables

Design variables	Upper bound/m	Lower bound/m
X_1	−0.04	0.04
Y_1	−0.04	0.04
Y_2	−0.04	0.04

30 sample points were selected in the design space using the optimal Latin hypercube method, and their distribution is illustrated in Fig. 18.

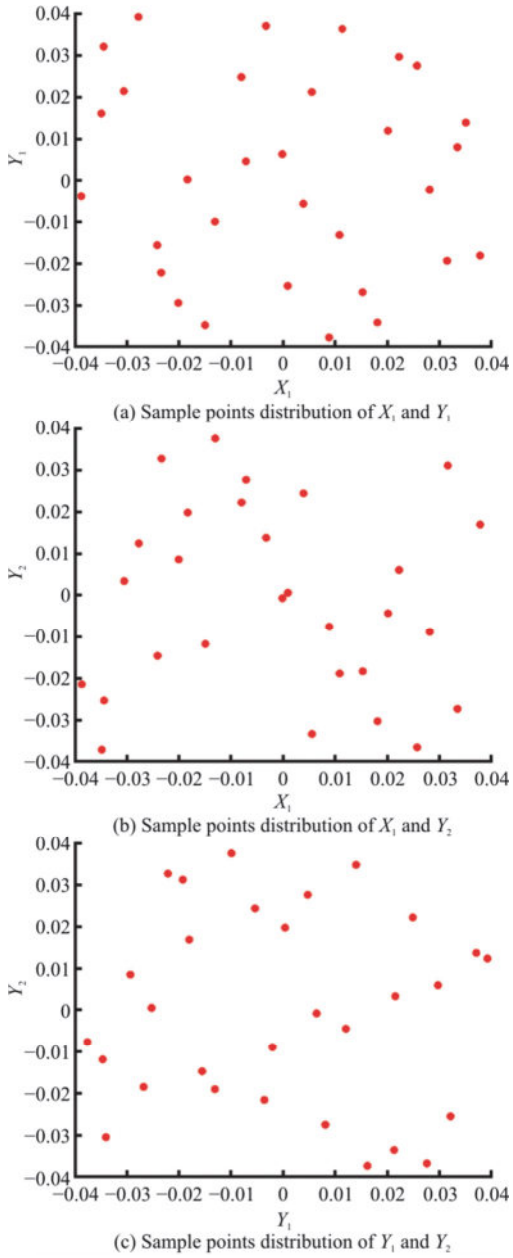


Fig. 18 Distribution of sampling points of three deformation parameters in the design space

2.3 *Optimization results discussion and analysis*

Numerical calculations were conducted on 30 sample hull forms using the two-phase flow CFD viscous flow solver. Through numerical calculations, a hydrodynamic performance dataset (including resistance and stern wake data) of JBC under different forms was obtained. A Kriging model was constructed to establish the nonlinear mapping relationships between the design variables and the objective functions 1 (resistance) and 2 (inflow non-uniformity). To ensure that the parameters selected for the Kriging models meet the accuracy requirements and that the constructed Kriging models are not affected by the selection of sample points, the leave-one-out cross-validation method was used to verify their stability. The results are shown in Fig. 19. It can be seen from the figure that the CFD-calculated values (f_{cal}) and the Kriging model-predicted values (f_{est}) of resistance and wake are consistent. For resistance, the Root Mean Square Error (RMSE) between the calculated and predicted values for all samples is 1.09×10^{-4}. For inflow non-uniformity, the RMSE between the calculated values and predicted values of all samples is 4.00×10^{-3}. Both accuracies meet the requirements, indicating that the constructed Kriging models are relatively stable.

The coefficient of determination (R^2) is utilised to evaluate data correlation and further illustrate the correlative relationship between calculated and predicted values. The R^2 of resistance data is 0.988, and the R^2 of wake non-uniformity data is 0.992.

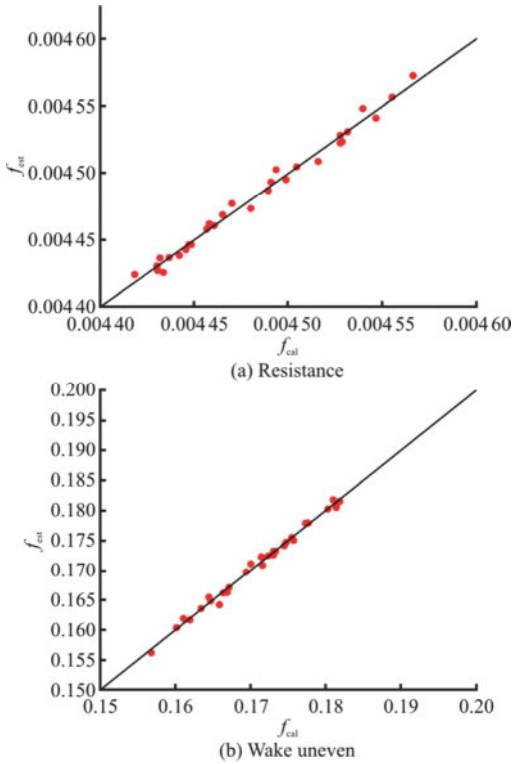


Fig. 19 Resistance and wake non-uniformity cross-validation

After determining the parameter settings of the Kriging surrogate models suitable for each objective, the multi-objective genetic algorithm NSGA-II was used to optimize the two objectives. The Pareto front–i.e. the set of all non-dominated solutions of the two surrogate models–was obtained through iteration, as illustrated in Fig. 20. The drag coefficient of the

initial hull form is 4.5×10^{-3}, and its inflow non-uniformity is 0.165 62. All dominated solutions on the Pareto front outperform the initial hull form in terms of both resistance and wake. Three optimized configurations that outperformed the initial hull form were selected from the Pareto front: Opt1, Opt2, and Opt3. Their corresponding optimal deformation parameters are presented in Table 6.

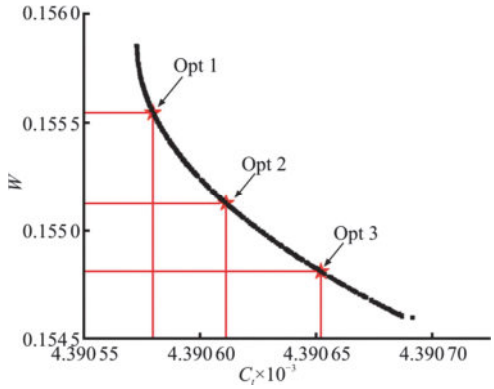


Fig. 20 Pareto frontier of resistance and non-uniform wake

Table 6 Optimal design variables

Design variables	X_1 / m	Y_1 / m	Y_2 / m
Opt 1	–0.039 99	0.035 541	0.039 999
Opt 2	–0.039 99	0.037 852	0.039 999
Opt 3	–0.039 99	0.039 131	0.039 999

By combining the deformation regions and deformation directions controlled by the design variables identified in Fig. 16, it can be known that: X_1 controls the movement of the stern lines along the ship's length direction, where negative values indicate movement toward the bow direction. Y_1 controls the width of the stern lines at the mid-section in the z-direction, where positive values indicate that the hull bottom becomes slenderer; Y_2 controls the width of the stern lines at the bottom section in the z-direction, where positive values indicate that the hull bottom becomes slimmer.

For the three optimized hull forms, both X_1 and Y_2 lie on the boundaries of the design space. It indicates that the slenderness of the stern flow-off stern lines and the hull bottom lines is conducive to reducing resistance and improving wake quality. It can be concluded that as the hull becomes slimmer, the hull's wetted surface area decreases, and thus the frictional resistance decreases correspondingly. Through measurement, compared with the wetted surface area of the initial hull form, the wetted surface areas of the three optimized hull forms have decreased by 1.728%, 1.761%, and 1.781%, respectively. However, constrained by the displacement volume and wetted surface area, the design space could not be expanded further–this ensures that the optimized hull forms meet practical building requirements.

Based on the optimal deformation parameters, three optimized hull forms were generated using the FFD volume mesh deformation module. Only the stern lines were deformed, and the stern lines of different cases were compared with those of the initial hull form, as shown in Fig. 21.

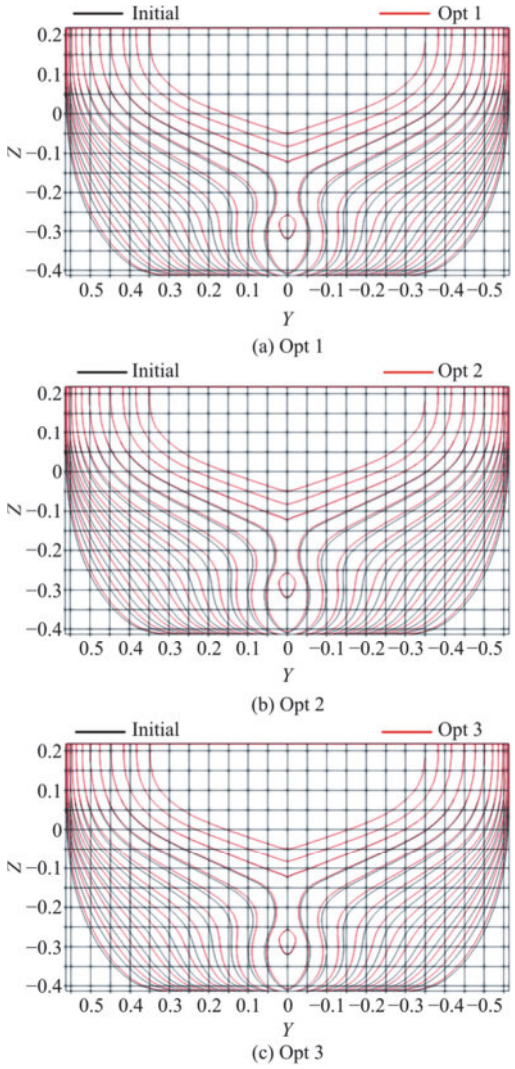


Fig. 21 Cross-section line comparison of stern form

Table 7 shows that the final CFD verification results for the three selected optimized hull forms are relatively consistent with theoretical values, indicating that the constructed multi-objective Kriging models accurately capture the nonlinear relationships between design parameters, resistance, and stern wake within the design space. The volume change rates corresponding to the Opt 1, Opt 2, and Opt 3 hull form cases are 1.18%, 1.21%, and 1.09%, respectively. The resistance optimization amplitude is approximately 2% to 3%. Since the CFD settings for both the optimized and initial hull forms are identical, the data are gua-

Table 7 Optimal results summary

Item	Resistance			Non-uniformity		
	Prediction ($\times10^{-3}$)	CFD ($\times10^{-3}$)	Opt/%	Prediction ($\times10^{-3}$)	CFD ($\times10^{-3}$)	Opt/%
Initial	-	4.50	-	-	0.165 6	-
Opt1	4.390 58	4.390 26	2.43	0.155 5	0.153 4	7.3
Opt2	4.390 61	4.394 22	2.35	0.155 1	0.153 9	7.1
Opt3	4.390 65	4.390 75	2.42	0.154 8	0.154 2	6.9

Table 8 Efficiency comparison of volume mesh deformation

Item	Mesh generation sequentially	Mesh deformation method
Sample number	30	30
Mesh number	6.824×10^6	6.824×10^6
CPU number	8 CPU (parallel)	8 CPU (parallel)
Time cost for a sample/h	0.25	0.008
Total time cost/h	7.5	0.24
Efficiency improvement/%	96.8	96.8

ranteed to lie within the same error space. Additionally, the topological structure of the volume mesh for the optimized hull forms is consistent with that of the initial hull form. Therefore, the optimization results are reliable.

By comparing the CFD verification results with the original initial hull form calculations, it is found that the hydrodynamic performance of the three optimized hull forms is improved, with a maximum reduction in resistance of 2.43%. The maximum reduction in wetted surface area is 1.781%, indicating that the frictional resistance has been thereby reduced. Meanwhile, modifying the stern lines has also reduced the hull's pressure drag. For the propeller disk wake at $x / L_{pp} = 0.984\,3$, the maximum improvement is 7.33%.

Quantitative comparison reveals the following conclusions:

(1) The volume mesh deformation method used has stable and reliable optimization performance in practical hull form optimization. The FFD-based volume mesh deformation technology has broad application prospects for optimizing hull form hydrodynamic performance.

(2) Volume mesh deformation can significantly improve the efficiency of ship hydrodynamic shape optimization. Statistics show that the parallel mesh generation time for a single sample is 15 min (8 cores). Therefore, when there are 30 samples, the time consumed for sequential parallel mesh generation of each sample is approximately 7.5 h. However, with volume mesh deformation, 30 sample meshes can be generated in a single parallel process using the FFD-based method (based on the initial hull form's mesh), with a total time of 0.24 h. The efficiency of this part is approximately 96.8% higher than that of the traditional method, as shown in Table 8.

(3) Compared with the initial hull form, the FFD-based volume mesh deformation method ensures that the numerical mesh topological structure of each sample hull form is consistent with that of the initial hull form. It avoids numerical errors caused by differences in topological structure resulting from independent mesh generation for each sample hull form. Therefore, the application of the FFD-based volume mesh deformation method also ensures the reliability of the final calculation results and optimization results.

An analysis of the optimization theory for differences between the optimized and initial hull forms will be conducted from various perspectives. From aspects including the flow field, vortex structure, and wake field, a qualitative and quantitative analysis will be performed on the influence mechanism of the changes in the stern configuration of the JBC hull form on the flow field–this aims to explore the methods for drag reduction and flow quality improvement of the JBC hull form.

2.4 *Physical field analysis of optimal hull forms*

Figure 22 shows the differences in the relative pressure distribution within the stern deformation region between the initial hull form and the three optimized hull forms. From the figure, it can be observed that the differences in pressure distribution among the three optimized hull forms are very small–the optimal deformation parameters corresponding to the three hull forms are close.

When analyzing the initial hull form and the optimized hull forms (as shown in the red-boxed area), changes in the stern lines significantly affect the distribution of the stern pressure gradient in the JBC hull form. The figure shows that the initial hull form has more pressure contour lines in the red-boxed area, and the changes in these lines are relatively steep. It

indicates that the pressure changes in this region cannot ensure a smooth transition. When the fluid flows along the pressure gradient, turbulence in this region is relatively high. For the optimized hull forms, after optimization, the stern lines of the hull become more slender, which alleviates the changes in the stern pressure gradient (compared with the initial hull form). As a result, the flow becomes more stable and orderly. Additionally, the slenderness of the stern region reduces the wetted surface area, thereby decreasing frictional resistance. This resistance accounts for a large proportion of the total resistance, thereby optimizing the hull form's resistance performance.

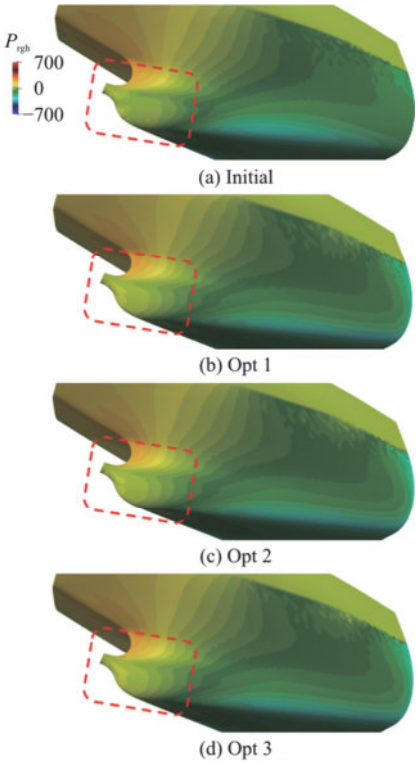


Fig. 22 Relative pressure distribution (p_{rgh}) for different optimization hull forms on the stern

To further reveal the flow field details at the stern and explore flow characteristics, the third-generation vortex identification method (Liutex) was used to reprocess the flow field in the stern deformation region[28-29]. The Liutex-based distribution of vortex structures at the hull stern is shown in Fig. 23. The picture shows the isosurface of the vortex structure, which is colored using the velocity field. Firstly, two small symmetric vortex tube structures behind the stern shaft can be observed within the yellow boxed area for all cases. Meanwhile, for the initial hull form, the vortex structures obtained using Liutex are also relatively disorganized behind the stern shaft (compared with those of the optimized hull forms). In the stern area, Liutex does not capture large-area small wall-attached vortex structures. It captures vortex tube structures near the hull bottom that extend to the hull stern. Liutex eliminates the influence of shear on vortex identification results. Thus, no large-area attached vortex structures are identified on the wall.

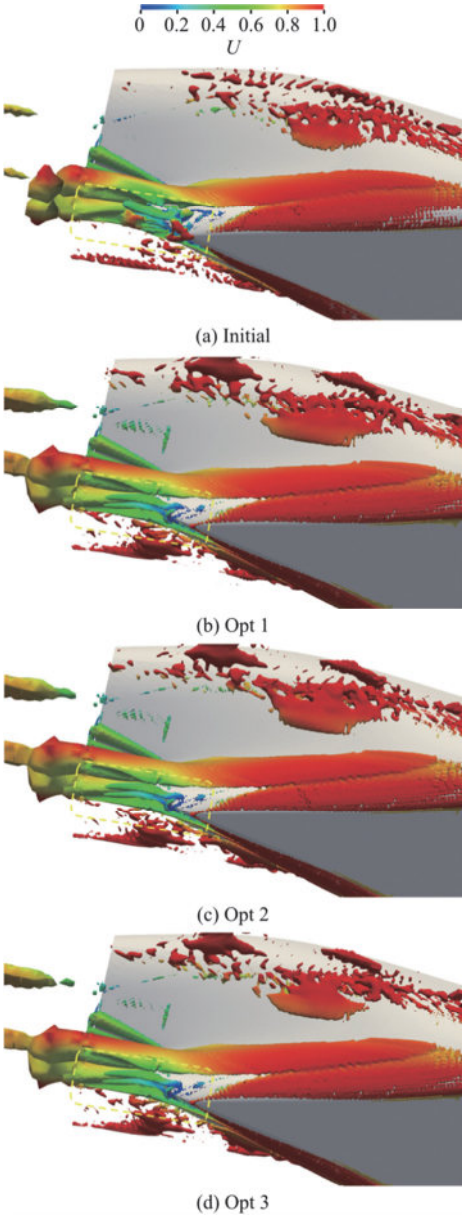


Fig. 23 Distribution of vortex structures in the ship stern based on Liutex (Liutex = 0.52)

After analyzing the macroscopic flow field in the stern region, the focus shifts to the influence of changes in the stern lines on the wake. Figure 24 shows the propeller disk wake conditions at section $x/L_{pp} = 0.984\,3$, rendered using the dimensionless quantity u/U ($U = 1.179$ m/s). The wake non-uniformity at the section $x/L_{pp} = 0.984\,3$ is one of the optimization objectives of this part. The most notable

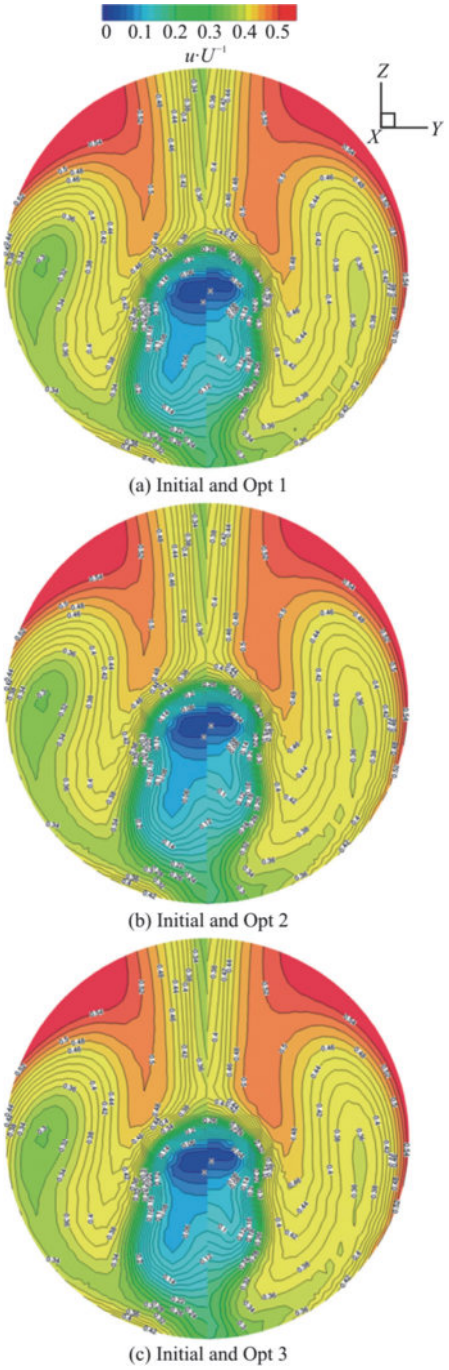


Fig. 24 Comparison of velocity at x/L_{pp}=0.984 3

difference at the propeller disk section x/L_{pp} = 0.984 3 is that the overall axial velocity in the optimized propeller disk region is increased. For the initial hull form, the value of u/U at the center of the "rabbit ear" is approximately 0.3, while for the optimized hull forms, u/U at the same position is above 0.36–this indicates that the velocity in the core region of the propeller disk is increased. In the central region of the propeller disk, compared with the initial hull form, the shape of the blue regions becomes more regular, and their area is relatively smaller. It shows that the flow at the center of the propeller shaft is more orderly, with reduced flow disturbance intensity and improved flow quality. Regarding the velocity gradient at the "rabbit ear" positions, it can be seen that the spacing between the optimized velocity contour lines increases, the velocity gradient is gentler, and the wake uniformity improves.

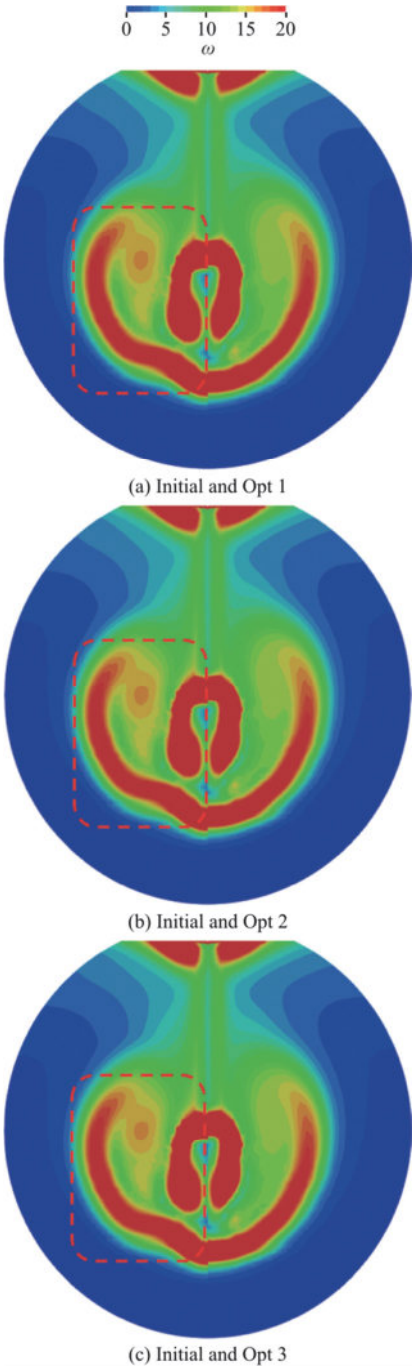
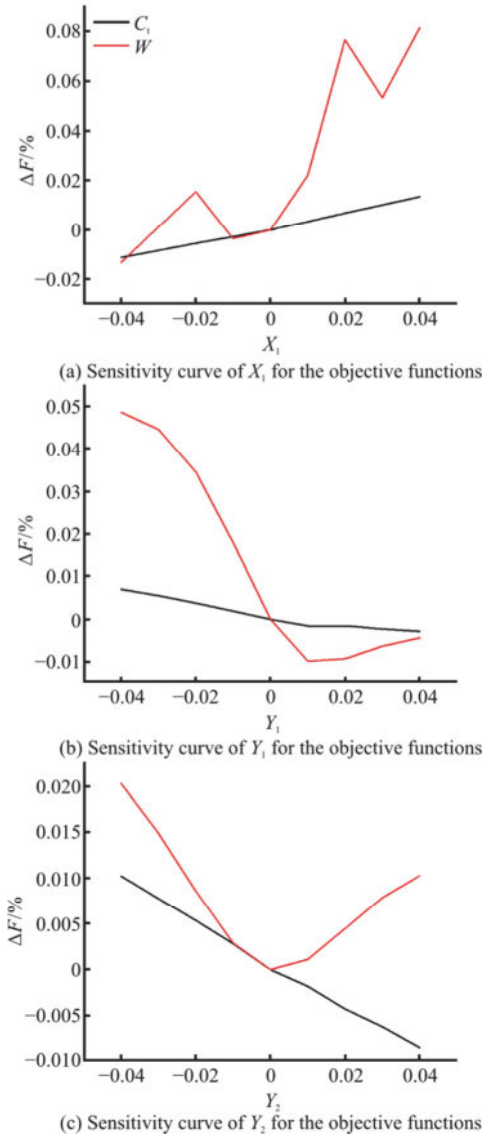


Fig. 25 Comparison of vorticity at x/L_{pp}=0.984 3

Figure 25 shows the propeller disk vorticity distributions at x/L_{pp} = 0.984 3. At the section x/L_{pp} = 0.984 3, focusing on the comparison within the red boxed area, similar to the situation at the section

$x / L_{pp} = 0.984\,3$, the vortex flow condition of the propeller disk is also improved through optimization, and the flow quality is enhanced.

Based on the above analysis, a parameter sensitivity analysis was conducted to examine the sensitivity of the objective functions ($\Delta F\%$) to the design variables, as shown in Fig. 26. The figure illustrates the sensitivity of the three design variables to Objective Function 1 (resistance) and objective function 2 (inflow non-uniformity). First, focusing on the impact of the three deformation parameters on resistance: As shown in the figure, when X_1 is positive, the stern lines become slimmer, the contraction curvature of the stern flow-off part increases, and flow separation at the stern is aggravated–this leads to increased pressure drag, and thus the resistance shows an increasing trend.



(a) Sensitivity curve of X_1 for the objective functions

(b) Sensitivity curve of Y_1 for the objective functions

(c) Sensitivity curve of Y_2 for the objective functions

Fig. 26 Sensitivity analysis of the design variables

In contrast, the relationship between Y_1 / Y_2 and resistance follows the same trend: as the stern becomes slimmer, resistance decreases. However, the width of the hull bottom lines controlled by Y_2 has a more significant impact on resistance. It may be because, while reducing flow separation, Y_2 also reduces the wetted surface area of the hull bottom and the stern–thus exerting a more significant impact on resistance.

For the propeller disk inflow non-uniformity, its relationship with the three deformation parameters is more complex, suggesting a complex correlation between changes in the stern line and propeller inflow.

Variable X_1: The forward shift of the stern line intensifies flow separation around the stern, thereby sharply increasing the inflow non-uniformity, with a decrease in wake quality of approximately 8%. When the stern line shifts backward, the wake non-uniformity first decreases, then increases, and then decreases again.

Variable Y_1: As the stern line changes from "bulky" to "slender", the inflow non-uniformity first decreases and then increases. It indicates that a slimmer stern line is not necessarily more beneficial to the wake, rather, there is a nonlinear relationship between the two.

Variable Y_2: The changes in the mid-stern line controlled by Y_1 are beneficial to improving wake quality as the line becomes slender, but again, "the slimmer, the better" does not hold. In contrast, the changes in the hull bottom line controlled by Y_2 do not affect wake optimization, they only intensify the increase in inflow non-uniformity. Through sensitivity analyses of the objective functions with respect to the design variables, the impact of the stern line on hull resistance and wake non-uniformity can be initially understood.

3. Conclusions

In this paper, a volume-mesh deformation module based on the FFD method was developed and investigated. By integrating FFD theory with dynamic-mesh and mesh-optimization theories, an FFD-based volume mesh deformation module was constructed. This method enables the rapid generation of numerical computational meshes for hull forms while maintaining the high quality of the original meshes.

Based on the developed method, two-dimensional numerical meshes for the airfoil were first selected for deformation tests. S-shaped deformation was applied to the volume mesh of the NACA 0012

airfoil to test its mesh quality under complex deformation conditions. After the 2-D volume mesh tests, 3-D meshes were evaluated. The computational meshes for the DTMB 5415 model and the SUBOFF model were adopted, and the bow and stern regions of the SUBOFF were deformed using the developed FFD volume mesh deformation program. The boundary layer and mesh quality before and after deformation were compared, with mesh non-orthogonality and skewness as evaluation indicators. The results show that the mesh quality remains favorable before and after deformation, meeting the accuracy requirements for numerical computations.

To verify this method in hull form optimization, the JBC hull form was selected as the optimization objective. The proposed volume mesh deformation method was employed to conduct multi-objective optimization, with two key goals: minimizing hull resistance and reducing stern inflow non-uniformity. Compared with the traditional optimization process, approximately 96.8% of the time consumed in the mesh generation step was saved. A maximum resistance reduction of 2.43% was achieved. A maximum improvement of 7.33% was obtained in propeller disk wake quality at the section $x / L_{\mathrm{pp}} = 0.9843$. Based on the optimization results, multiple flow-field visualization techniques were applied to conduct a comprehensive comparative analysis of the three optimized hull forms and the initial hull form. The underlying principles of flow optimization were summarized. A preliminary analysis of the sensitivity between design variables and objective functions was conducted.

Improving optimization efficiency is an important research direction in hull form optimization. In this paper, a volume mesh deformation method based on Free-Form Deformation is developed to further enhance the efficiency of hull form optimization while ensuring satisfactory optimization performance. Nevertheless, this study still has certain limitations. The proposed method can currently construct only regular rectangular deformation control volumes, and its deformation control capability for complex geometries needs to be further improved. In future work, the applicable scope of the volume mesh deformation program will be extended on the existing foundation. Meanwhile, the theoretical research, benchmark tests, and practical applications presented in this paper lay the foundation for the subsequent development of more efficient hull-form optimization tools.

Conflict of interest

All authors declare that there are no other competing interests.

References

[1] Chen S. Gradient-based aerodynamic shape optimization design methods and applications [D]. Doctoral Thesis, Xi'an: Northwestern Polytechnical University, 2016(in Chinese).

[2] Rendall T C S, Allen C B. Efficient mesh motion using radial basis functions with data reduction algorithms [J]. *Journal of Computational Physics*, 2009, 228(17): 6231-6249.

[3] Liu X, Qin N, Xia H. Fast dynamic grid deformation based on Delaunay graph mapping [J]. *Journal of Computational Physics*, 2006, 211(2): 405-423.

[4] Hu Z, Yuan Y, Xiong D, et al. An efficient multidomain RBF mesh deformation method based on MPI/OpenMP hybrid parallel interpolation [J]. *Journal of Computational Physics*, 2025, 537: 114113.

[5] de Boer A, van der Schoot M S, Bijl H. Mesh deformation based on radial basis function interpolation [J]. *Computers & Structures*, 2007, 85(11-14): 784-795.

[6] Liao H. Research on unstructured mesh deformation technology based on SVR [D]. Doctoral Thesis, Changsha, China: National University of Defense Technology, 2020(in Chinese).

[7] Luke E, Collins E, Blades E. A fast mesh deformation method using explicit interpolation [J]. *Journal of Computational Physics*, 2012, 231(2): 586-601.

[8] Zhao Z, Ma R, He L, et al. An efficient large-scale mesh deformation method based on MPI/OpenMP hybrid parallel radial basis function interpolation [J]. *Chinese Journal of Aeronautics*, 2020, 33(5): 1392-1404.

[9] Stannard A, Qin N. Hybrid mesh deformation for aerodynamic-structural coupled adjoint optimization [J]. *AIAA Journal*, 2022, 60(6): 3438-3451.

[10] Hsu S Y, Chang C L, Samareh J. A simplified mesh deformation method using commercial structural analysis software [C]//*10th AIAA/ISSMO Multidisciplinary Analysis and Optimization Conference*. Albany, USA, 2004: 1197-1218.

[11] Salmoiraghi F, Scardigli A, Telib H, et al. Free-form deformation, mesh morphing and reduced-order methods: Enablers for efficient aerodynamic shape optimization [J]. *International Journal of Computational Fluid Dynamics*, 2018, 32(4-5): 233-247.

[12] Morelli M, Bellosta T, Guardone A. Efficient radial basis function mesh deformation methods for aircraft icing [J]. *Journal of Computational and Applied Mathematics*, 2021, 392: 113492.

[13] Secco N R, Kenway G K W, He P, et al. Efficient mesh generation and deformation for aerodynamic shape optimization [J]. *AIAA Journal*, 2021, 59(4): 1151-1168.

[14] Zhao R, Li C, Guo X, et al. A parallel iteration algorithm for greedy selection based IDW mesh deformation in OpenFOAM [C]//*2019 3rd International Conference on Electronic Information Technology and Computer Engineering (EITCE)*, Xiamen, China, 2019: 1449-1452.

[15] Villa D, Furcas F, Pralits J O, et al. An effective mesh deformation approach for hull shape design by optimization [J]. *Journal of Marine Science and Engineering*, 2021, 9(10): 1107.

[16] Jeong K L, Jeong S M. A mesh deformation method for CFD-based hull form optimization [J]. *Journal of Marine Science and Engineering*, 2020, 8(6): 473.

[17] Demo N, Tezzele M, Mola A, et al. Hull shape design

optimization with parameter space and model reductions, and self-learning mesh morphing [J]. *Journal of Marine Science and Engineering*, 2021, 9(2): 185.

[18] Nazemian A, Ghadimi P. Shape optimisation of trimaran ship hull using CFD-based simulation and adjoint solver [J]. *Ships and Offshore Structures*, 2022, 17(2): 359-373.

[19] He P, Filip G, Martins J R R A, et al. Design optimization for self-propulsion of a bulk carrier hull using a discrete adjoint method [J]. *Computers & Fluids*, 2019, 192: 104259.

[20] Li S, Zhu F, Hou X, et al. Application of mesh deformation and adaptive method in hullform design optimization [J]. *Journal of Marine Science and Technology*, 2022, 27(1): 566-575.

[21] Liu Z, Liu W, Chen Q, et al. Resistance reduction technology research of high speed ships based on a new type of bow appendage [J]. *Ocean Engineering*, 2020, 206: 107246.

[22] Kim H, Yang C, Noblesse F. Hull form optimization for reduced resistance and improved seakeeping via practical designed-oriented CFD tools [C]//*Proceedings of the Grand Challenges in Modeling & Simulation*, Ottawa, Canada, 2010.

[23] Liu X, Wan D, Chen G, et al. Wigley hull form optimization with or without bulbous bow [C]//*Proceedings of the 29th International Ocean and Polar Engineering Conference (ISOPE 2019)*, Honolulu, USA, 2019: 4486-4494.

[24] Sederberg T W, Parry S R. Free-form deformation of solid geometric models [J]. *Computer Graphics (ACM)*, 1986, 20(4): 151-160.

[25] Löhner R, Yang C. Improved ALE mesh velocities for moving bodies [J]. *Communications in Numerical Methods in Engineering*, 1996, 12(10): 599-608.

[26] Wu P, Chang C, Huang Y. Design of energy-saving duct for JBC to reduce ship resistance by CFD method [J]. *Energies*, 2022, 15(17): 6484.

[27] Islam H, Guedes Soares C. Uncertainty analysis in ship resistance prediction using OpenFOAM [J]. *Ocean Engineering*, 2019, 191: 105805.

[28] Chu X, Jiang S, Zhu J, et al. Liutex-shear interaction in Lamb-Oseen vortex and three-dimensional cylinder flow at Re = 3 900 simulated with SWLBM [J]. *Journal of Hydrodynamics*, 2025, 37(2): 230-238.

[29] Wang Y, Yu H, Zhao W, et al. Liutex-based vortex control with implications for cavitation suppression [J]. *Journal of Hydrodynamics*, 2021, 33(1): 74-85.